

# **A machine-learning approach for detection of local brain networks and marginally weak signals identifies novel AD/MCI differentiating connectomic neuroimaging biomarkers**

Yanming Li<sup>1</sup>, Jian Kang<sup>2</sup>, Chong Wu<sup>3</sup>, Ivo D. Dinov<sup>4</sup>, Jinxiang Hu<sup>1</sup>, Prabhakar Chalise<sup>1</sup>, Jonathan D. Mahnken<sup>1</sup>, for the Alzheimer's Disease Neuroimaging Initiative

1. Department of Biostatistics & Data Science, University of Kansas Medical Center, Kansas City, KS, USA
2. Department of Biostatistics, University of Michigan, Ann Arbor, MI, USA
3. Department of Statistics, Florida State University, Tallahassee, FL, USA
4. Departments of Computational Medicine and Bioinformatics, and Health Behavior and Biological Sciences, University of Michigan, Ann Arbor, MI, USA

**Corresponding to:** Yanming Li, Department of Biostatistics , Data Science, University of Kansas Medical Center, Kansas City, KS, USA. Email: [yli8@kumc.edu](mailto:yli8@kumc.edu).

## Abstract

**Introduction:** A computationally fast machine learning method is introduced for uncovering the whole-brain voxel-level connectomic spectra that differentiates different status of Alzheimer's disease (AD). The method is applied to the Alzheimer's Disease Neuroimaging Initiative (ADNI) Fluorine-fluorodeoxyglucose Positron Emission Tomography (FDG-PET) imaging and clinical data and identified novel AD/MCI differentiating connectomic neuroimaging biomarkers.

**Methods:** A divide-and-conquer algorithm is introduced for detect informative local brain networks at voxel level and whole-brain scale. The connection information within the local networks is integrated into the node voxels, which makes detection of the marginally weak signals possible. Prediction accuracy is significantly improved by incorporating the local brain networks and marginally weak signals.

**Results:** Brain connectomic structures differentiating AD and mild cognitive impairment (MCI), AD and healthy, and MCI and healthy were discovered. We identified novel AD/MCI-associated neuroimaging biomarkers by integrating local brain networks and marginally weak signals. For example, network-based signals in paracentral lobule ( $p$ -value= $6.1e-5$ ), olfactory cortex ( $p$ -value= $4.6e-5$ ), caudate nucleus ( $1.8e-3$ ) and precentral gyrus ( $1.8e-3$ ) are informative in differentiating AD and MCI. Connections between calcarine sulcus and lingual gyrus ( $p$ -value=0.049), between parahippocampal gyrus and Amygdala ( $p$ -value=0.025), between rolandic opercula and insula lobes ( $p$ -values=0.0028 and 0.0026). An overall prediction accuracy of 95.3% was achieved by integrating the selected local brain networks and marginally weak signals, compared to 84.0% by not considering the inter-voxel connections and using marginally strong signals only.

**Conclusion:** (i) The connectomic structures differentiating AD and MCI are significantly different to that differentiating MCI and healthy, which may indicate different neuronal etiology for AD and MCI. (ii) Many neuroimaging biomarkers exert their effects on the outcome diseases through their connections to other markers. Integrating such connections can help identify novel neuroimaging biomarkers and improve disease prediction accuracy.

## 1. Introduction

Alzheimer's disease (AD) ranks the third as a cause of death for people 75 and older<sup>1,2</sup>. Every 65 seconds, someone in the US develops AD<sup>3</sup> and it afflicted around 5.8 million Americans in 2020<sup>4</sup>. Overall, AD is considered the most expensive disease<sup>5</sup> in US, with the overall cost of the disease being \$305 billion in the U.S. in the year 2020<sup>4</sup>. Before the onset of AD, individuals may experience an intermediate cognitive deterioration known as mild cognitive impairment (MCI) that are not severe enough to interfere with their daily activities. As the earliest detectable clinical stage toward AD, MCI provides an attractive checkpoint of disease-modifying intervention<sup>6,7</sup>. Compared to AD, MCI is more subtle and difficult to prognosis<sup>8,9</sup>. Early and accurate prediction of MCI and differentiating neuropathology of MCI and that of AD is crucially important for successful treatment development and precision prevention<sup>10,11,12,13</sup>.

Many cognitive tests have been developed for AD diagnosis<sup>14</sup>. However, these tests have certain limitations. For example, cognitive tests are often powerless in discriminating subtle differences between AD and MCI and between MCI and healthy. Also, cognitive tests cannot be used for novel neuroimaging biomarker discovery that may provide insights on underlying neuropathology.

High-resolution neuroimaging scans nowadays provide unparalleled precision for discovering AD (MCI) associated neuroimaging biomarkers. For example, Positron Emission Tomography (PET) images<sup>15,16,17</sup> have been successfully used to understand the neurodegenerative mechanisms<sup>18</sup>. Most of current methods focus on identifying the locales and individual values of imaging biomarkers, such as important voxels, hotspots or brain regions associated with a disease<sup>19,20,21</sup>, while ignoring the connectivity between markers. The number of potential connections between tens of thousands of voxels in a neuroimage is often of astronomical scales. For example, each ADNI PET scan used in our study consists of more than 185,000 voxels. Jointly inferring all potential connections between these voxels accounts to inverting a covariance matrix of dimension 185,000×185,000, which has a computational

complexity of  $O(185,000^{2.375})^{22}$ . Even with very powerful computing tools, it is infeasible to invert such a large-dimensional matrix.

Even though extremely challenging, detection of voxel-level brain connectomes associated with AD has attracted much interest. First, both AD and MCI can be viewed as a connectomic disorder neuropathologically, in the sense that their onset is often accompanied with not only the loss of brain matters itself, but also the reduction of inter-neuron fiber connectivity required for healthy cognitive functioning<sup>23,24</sup>. Brain connectomics, which models the whole brain as a spectrum of network circuits, provides a systematic view to AD neuropathology and have been increasingly used to link the diseases with structural and functional neuroimages<sup>25</sup>. Most existing brain connectomic networks are region-based functional networks, which aggregate neurons into priori-defined functionally related or spatially circumscribed regions of interest (ROIs)<sup>26,27,28,29</sup>. While the current neuropathological theories, such as beta-amyloid initiated senile plaques and tau-protein initiated neurofibrillary tangles, indicate that developments of AD and MCI are more directly related to breaks-down of connectivity at neuronal level, other than at regional level. Such connectomic patterns are more reflected in the voxel-level connections<sup>30,31</sup>. Region-based methods often lead to a loss of information and inferior prediction performance.

Another advantage of detecting inter-voxel connections is about prediction. As we will demonstrate shortly, a large portion of the predictiveness for AD is embedded in the connections between voxels. In fact, AD-risk imaging biomarkers currently identified explain only a small proportion of the disease variation<sup>32,33,34</sup>. More novel neuroimaging biomarkers are yet to be discovered. Integrating connections between voxels into the disease prediction makes the detection of marginally weak signals possible. The marginally weak signals have small power in differentiating the disease status and are not detectable by themselves. They are, therefore, usually ignored in contemporary neuroimaging

association studies. However, when taken into consideration their connections with other signals, marginally weak signals could exude strong predictive effects<sup>35,36</sup>.

Such a case is illustrated in Figure 1. The left panel depicts a local brain-network in cerebellum crus on the left hemisphere consisting of twelve voxels. The network contains two marginally detectable voxels “vox 94316” and “vox 98031”. All other ten voxels are marginally weak and undetectable. The right-panel table in Figure 1 gives the marginal and local-network-adjusted mean differences between the AD and MCI groups. The first column lists the marginal mean differences (divided by the marginal standard deviations) without considering the connections between the voxels. The second column lists the local-network-adjusted mean differences. The local-network-adjusted mean difference for a voxel integrates its connective information with other voxels, such as the number of edges connected to it, the strength of these connections and marginal differentiating power of its connected voxels. The discriminant power of most of the ten marginally undetectable signals are significantly boosted up by incorporating their connective information. All the ten marginally weak voxels become more powerful in differentiating AD and MCI than the two marginally strong signals after adjusting for the local network structure.

[Figure 1 about here]

In this work, we analyzed the ADNI Fluorine-fluorodeoxyglucose (FDG)-PET imaging and clinical data by detecting local brain networks and marginally weak signals<sup>36</sup>. To the best of our knowledge, this is the first whole-brain voxel-level connectivity study in the literature. The identified connectomic signatures were then integrated into AD/MCI prediction. Our approach avoids ultrahigh-dimensional precision matrix calculation by disassembling the whole brain connectome into disjoint local brain networks. It is highly efficient in computation. By integrating the voxel-level connectivity and marginally weak signals, the prediction accuracy has been significantly improved. Moreover, meaningful biological interpretation

about identified network-based signatures can be made based on our findings, which might help to advance our understanding on the mechanisms of MCI and AD.

The rest of the paper is organized as following. Section 2 introduces the methods for detection of predictive local brain networks and marginally weak signals, and prediction rules for classifying the diseases. Section 3 introduces the ADNI PET imaging datasets. Section 4 gives the analysis results and biological annotations for our findings. The paper is concluded by Section 5, where a brief discussion of relevant issues is provided.

## 2. Methods

Figure 2 depicts the major steps of our analysis pipeline. Details for the methods used are elaborated next.

[Figure 2 about here]

### 2.1. Notations

Let  $X = (X_1, \dots, X_p)'$  be the stacked vector for the intensity scores of all  $p$  voxels in an imaging scan. Denote by  $X_i = (X_{i,1}, \dots, X_{i,p})'$  the observed  $X$  vector from subject  $i$ . Let  $Y_i$  be the class indicator (coded as 0, 1, 2 for healthy, MCI and AD, respectively) for subject  $i$ ,  $i = 1, \dots, n$ , where  $n$  is the total number of subjects. Denote by  $X = (X_1', \dots, X_n')'$  the  $n \times p$  data matrix. Denote by  $n_k$  the size of class  $k$ ,  $k = 0, 1, 2$ . Denote by  $G = (V, E)$  the whole brain connectomic network, with a vertex set  $V \equiv \{1, \dots, p\}$  and an edge set  $E$ . A connection (or an edge)  $(j, j_0)$  exists between two voxels  $j$  and  $j_0$  if and only if voxels  $X_j$  and  $X_{j_0}$  are conditionally dependent given all other voxels. Note that connection (or an edge) between two voxels is essentially different than the correlation between them. The former is a joint concept depending

on all the other voxels, while the latter is a marginal concept depending only on the pair of voxels under consideration.

## 2.2. Detection of marginally strong signals

Marginal two sample t-tests are used to select marginally strong signals, which each differentiates a pair of classes by itself. Specifically, for each feature  $j, j = 1, \dots, p$ , we calculate

$$\hat{T}_j(k, k') = (\bar{X}_j^{[k]} - \bar{X}_j^{[k']}) / s_{\Delta} \quad (1)$$

for a class pair  $(k, k')$ ,  $k \neq k'$ , in  $\{0, 1, 2\}$ . Here  $\bar{X}_j^{[k]} = (1/n_k) \sum_{Y_i=k} X_{i,j}$  and  $s_{\Delta} = \sqrt{\sum \sum (X_{i,j} - \bar{X}_j^{[l]})^2 / (n_k + n_{k'})}$ . The first  $\tau \leq n$  features with the highest  $|\hat{T}_j(k, k')|$  values are selected as the marginally strong signals. Here  $\tau$  is a tuning parameter and can be selected by data-driven procedures such as cross-validation.

## 2.3. Detection of predictive local brain networks

Under the assumption that the  $p$  voxels follow a multivariate normal distribution with a mean vector  $\mu$  and a covariance matrix  $\Sigma$ , The network  $G$  can be characterized by the precision matrix  $\Omega = \Sigma^{-1}$ . An edge  $(j, j')$  exists if and only if the  $(j, j')$ th entry of  $\Omega$ , denoted by  $\Omega_{jj'}$ , is nonzero and the strength of the edge equals to the magnitude of  $\Omega_{jj'}$ . As stated before, jointly estimating the whole  $\Omega$  matrix of all 185,000 voxels is computationally prohibitive. Here we employed a “divide-and-conquer” algorithm introduced in Li et al.<sup>36</sup>, to detect the local brain networks. The local networks are much smaller in size and thus their corresponding precision matrices are much easier to calculate. Assume that each local brain network contains at least one marginally strong voxel. These marginally strong voxels serve as hubs in the local networks. For each marginally strong signal detected, we look for the set of voxels connected to it, either directly through an edge or indirectly through a path consisting of a series of edges. That is, to find the connected component in  $\Omega$  containing it. However, it is impossible to detect

such connected components without knowing  $\Omega$ . Utilizing a statistical property which states that the connected component structure of  $\Omega$  can be asymptotically recovered by that of the thresholded sample correlation matrix,  $\tilde{R} \equiv \hat{R} 1(|\hat{R}_{jj'}| > \alpha)^{37,38}$ , we can detect the connected components in  $\tilde{R}$  instead. Here  $\hat{R}$  is the estimated sample correlation matrix and  $\hat{R}_{jj'}$  is its  $(j, j')$ th entry and 1 is the indicator function. The thresholding parameter  $0 < \alpha < 1$  controls the sparsity of  $\tilde{R}$ . The computational complexity of  $\tilde{R}$  is orders of magnitude lighter than that of estimating  $\Omega$ . Moreover, since the correlations can be estimated pairwise, they can be calculated in a parallel way on multi-core computer clusters.

Recursive labeling algorithm<sup>39</sup> is employed in detecting the connected component in  $\tilde{R}$  for each marginally strong signal. Denote by  $C_l$ ,  $l = 1, \dots, B$ , the  $B$  connected components identified. Each  $C_l$  indexes a local brain network. Let  $\hat{\Sigma}_{C_l}$  be the sub-sample covariance matrix corresponding to the set  $C_l$ . The precision matrices  $\hat{\Omega}_{C_l} = \hat{\Sigma}_{C_l}^{-1}$  characterize the topology for the corresponding local networks. Sizes of  $C_l$ s can be controlled by carefully choosing the thresholding parameter  $\alpha$ .

## 2.4. Detection of marginally weak signals

Local-network-adjusted effects are then calculated for voxels within each  $C_l$ . Specifically, for each  $C_l$ , the following network-adjusted statistics vector is calculated:

$$\hat{T}_{C_l}^{net}(k, k') = \hat{\Omega}_{C_l}(\bar{X}_j^{[k]} - \bar{X}_j^{[k']}). \quad (2)$$

For each voxel  $j$  in  $C_l$ , its network-adjusted statistic is the corresponding entry in  $\hat{T}_{C_l}^{net}(k, k')$ . Specifically,

$$\hat{T}_j^{net}(k, k') = \sum_{j' \in C_l} [\hat{\Omega}_{C_l}]_{jj'} (\bar{X}_j^{[k]} - \bar{X}_j^{[k']}). \quad (3)$$

Compared to the marginal statistics  $\hat{T}_j(k, k')$  in (1), instead of standardizing by the marginal variation (measured in  $s_A$ ),  $\hat{T}_j^{net}(k, k')$  also adjusts for the local network connections for feature  $j$  (estimated in  $[\hat{\Omega}_{C_l}]_{jj'}$ s) and the marginal differential effects of voxels connected to feature  $j$  (measured in  $\bar{X}_j^{[k]} - \bar{X}_j^{[k']}$  for  $j' \neq j$  in  $C_l$ ).



Not all the voxels in  $C_l$ s are necessarily predictive. To reduce false positives, we further select predictive marginally weak signals within  $\cup_{l=1}^B C_l$ . The top ranked  $\nu$  voxels with the greatest  $|\hat{T}_j^{net}(k, k')|$  are selected, beside of the marginally strong signals. Here  $\nu$  is a tuning parameter controlling the size of marginally weak signal set. The predictive signals (both marginally strong and marginally weak), together with the local brain networks they are residing in, form the AD (or MCI) predictive brain connectome. Figure 3 gives a toy example about incorporating a local brain network into marginally weak signal detection.

[Figure 3 about here]

## 2.5. Assigning p-values to selected signals and local brain networks

A non-parametric permutation test is used to evaluate significance of selected signals<sup>40,41</sup>. Specifically, the p-value for a selected voxel  $j$  is calculated through the following procedure:

1. Calculate  $\hat{T}_j$  and  $\hat{T}_j^{net}$  using the original data. If voxel  $j$  was not selected, then  $\hat{T}_j^{net} = 0$ .
2. Randomly permute the class label vector  $(Y_1, \dots, Y_n)'$   $M$  times for some large number  $M$  and generate  $M$  permuted datasets.
3. For each feature  $j$ , calculate (2) using the  $m$ th permuted dataset, denoted by  $\hat{T}_j^{net(m)}$ ,  $m = 1, \dots, M$ .
4. Assign p-value to a selected voxel  $j$  to be

$$p_j = \frac{1}{M} \sum_{m=1}^M 1(|\hat{T}_j^{net(m)}| > |\hat{T}_j^{net}|).$$

To access significance of the network-based signatures identified, we assign network p-values to the selected local brain networks using the following Hotelling's T-squared distribution

$$\frac{n-c}{c(n-1)} (\bar{X}_{C_l}^{[k]} - \bar{X}_{C_l}^{[k']})' \hat{\Omega}_{C_l} (\bar{X}_{C_l}^{[k]} - \bar{X}_{C_l}^{[k']}) \sim F_{c, n_k + n_{k'} - c},$$

where,  $c$  is the number of voxels in  $C_l$  and  $F_{c, n_k + n_{k'} - c}$  is the F-distribution with parameters  $c$  and  $n_k + n_{k'} - c$ .

## 2.6 Disease status prediction

Let  $X_{new}$  and  $Z_{new}$  be the predictor vector and adjusting covariate vector for a new subject in the test dataset, respectively, then the class of the new subject can be predicted by the following rule.

$$\hat{Y}_{new} = \operatorname{argmax}_{k \in \{0,1,2\}} \left\{ (Z_{new} - \bar{Z}^{[k]}/2)' \hat{\Sigma}_Z^{-1} \bar{Z}^{[k]} + \sum_{l=1}^B (X_{new,C_l} - \bar{X}_{C_l}^{[k]}/2)' \hat{\Omega}_{C_l} \bar{X}_{C_l}^{[k]} \right\},$$

where  $X_{new,C_l}$  is the subvector of  $X_{new}$  indexed by  $C_l$ .

## 3. ADNI datasets

During the last two decades, large amount of neuroimaging, genetic and clinical data have been acquired in ADNI studies<sup>42,43,44</sup>. In this study, we used the ADNI phase-I FDG-PET baseline scans with 54 AD patients, 131 MCI patients and 72 healthy subjects to detect brain connectomic structures for AD and MCI prediction.

### 3.1 Data processing

Standard preprocessing steps including co-registration, normalization and spatial smoothing (8 mm full width at half maximum) were applied to the PET dataset. Each image is registered to a template with 185,405 active voxels embedded in a 91 x 109 x 91 3D-array. We further grouped the 185,405 voxels into 116 regions of interest (ROI) segmented by the automated anatomical labeling atlas<sup>45</sup>. ROI names and numbers are listed in the Table A1 in the Appendix.

## 4. Analysis and results

Pairwise correlations and covariances between all voxels were first calculated on parallel threads using a Hewlett-Packard workstation with 16 core Intel Xeon processors and a 256GB memory size.

Correlation matrix was then thresholded at 0.8 to retain only highly correlated voxels. To further reduce the computational burden, we set all entries within a thresholded correlation block between two ROIs to zeros if the average  $L_2$  norm ( $L_2$  norm divided by the number of nonzero entries in the block) of that block is  $\leq 0.4$ . Thus, only highly correlated ROIs were be considered. For example, For ROI 5, only its closely connected ROIs: ROI 6, 9, 15, 25, 26, 27 and 28, were considered in our analysis (see Figure 4-a). This correlation block structure represents an overarching region-level connectivity structure (Figure 4-b).

[Figure 4 about here]

Variable selection was performed separately within each highly correlated ROI clusters. Parallel computing was implemented for this step. We used  $\tau = 5$ ,  $\alpha = 0.8$  and  $\nu = 20$  on each ROI cluster to select local-brain networks, and marginally strong and weak signals that differentiated a pair of classes. When searching for the connected component of a marginally strong signal, we focused on the voxels that are connected to a marginally strong signal with a connection path less than 10 in length. We used  $M = 10,000$  in the non-parametric permutation tests. In total, 2,686 informative voxels were selected. Among them, 836 are marginally strong and 1,850 are marginally weak. There were 661 (302), 695 (306) and 610 (309) were marginally weak (marginally strong) signals for differentiating AD and MCI, AD and Healthy, and MCI and Healthy, respectively. There were 47 (61) marginally weak (marginally strong) signals that differentiate both AD-to-MCI and AD-to Healthy, 3 (0) marginally weak (marginally strong) signals that differentiate both AD-to-MCI and MCI-to-Healthy, 67 (20) marginally weak (marginally strong) signals that differentiate both AD-to Healthy and MCI-to-Healthy, and 1 marginally weak signal that differentiate all three pairs. The selected informative signals differentiating AD and MCI, AD and healthy, and MCI and healthy are sitting in 168, 129 and 122 local brain networks, respectively. Table 1 lists the top selected voxel signals that are informative in differentiating at least one pair of disease status. Figure 5 shows the top selected marginally weak signals, along with their marginal and

network-adjusted effects. Note that some regions identified containing mostly marginally weak signals have either not been reported to be associated with AD or MCI, or just been discovered recently, such as middle temporal gyrus<sup>46</sup>, olfactory bulbs<sup>47</sup>, lingual gyrus<sup>48</sup> and amygdala<sup>69</sup>. These novel findings demonstrate the power of our method in identifying novel neuroimaging biomarkers. Table 2 lists the top selected brain networks with a significant unadjusted p-values. Most of selected voxels would still be significant after adjusting for multiple tests. The topologies of these networks are depicted in Figure 6. For the sake of presentation, we only included 12 the most closely connected voxels to a marginally strong signal in each depicted network. The whole brain connectomic structure that differentiate AD and MCI is presented in Figures 7 and 8. Each cluster of arcs in Figure 7 represent connections within an ROI. Arcs run across different clusters represent connections between different ROIs. Figure 8 shows, on the other hand, the positions and overarching topologies of the detected connectome. The corresponding figures for connectomes that differentiate AD and healthy, MCI and healthy are provided in the Appendix.

[Figure 5 about here]

[Table 2 about here]

[Figure 6 about here]

[Figure 7 about here]

[Figure 8 about here]

For many of the local networks identified, associations between their residing ROI and AD status are supported by literature evidence. These threads of evidence are listed in the last column of Table 2. Our analysis showed that connections within paracentral lobule (p-value=6.1e-5), olfactory cortex (p-value=4.6e-5), caudate nucleus (1.8e-3) and precentral gyrus (1.8e-3) are informative in differentiating AD and MCI; Connections within cerebellum crus (p-value=0.03), lingual gyrus and calcarine sulcus

(p-value=3.8e-6) and amygdala (p-value=1.6e-8) are informative in differentiating AD and the healthy; Connections within precuneus gyrus (p-value=2.7e-7), middle temporal gyrus (p-value=1.6e-3), middle orbitofrontal cortex (p-value=0.014) and inferior parietal lobule (p-value=0.038) are informative in differentiating MCI and the healthy.

Connections across different ROIs that contribute to differentiating a pair of disease status are of particular interest, as they may indicate the functional connection that contributes to AD etiology. The following cross-ROI connections were identified for differentiating AD and MCI: connections between calcarine sulcus and lingual gyrus (network p-value=0.049), connections between parahippocampal gyrus and amygdala (network p-value=0.025), connections between rolandic opercula and insula lobes (network p-values=0.0028 in the left hemisphere and =0.0026 in the right hemisphere). The connections between calcarine sulcus and lingual gyrus (network p-value=7.5e-6) and connections between parahippocampal gyrus and amygdala (network p-value=1.7e-4), were also identified to differentiate AD and the healthy. Other significant cross-ROI networks that differentiate AD and the healthy, MCI and the healthy are listed in Table S2 in the Appendix.

The patterns of the selected connectomes differentiating the three disease pairs (AD-to-MCI, AD-to-healthy, and MCI-to-healthy) are significantly different. See Figure 8 and Figures A3 and A6 in the Appendix. While connections between calcarine sulcus and lingual gyrus, between parahippocampal gyrus and amygdala are informative for differentiating both AD-to-MCI and AD-to-healthy; connections between cingulum posterior, left hemisphere and cingulum posterior, right hemisphere, between cingulum middle, left hemisphere and cingulum middle, right hemisphere are informative for differentiating both AD-to-healthy and MCI-to-healthy. Note that there is no selected local network that differentiates both AD-to-MCI and MCI-to-healthy, which indicates that the development of MCI and the progression from MCI to AD may have different neuropathology pathways.

For prediction, we used five-fold cross-validation to divide the whole dataset into five parts with about the same sample sizes. Each time, we combined four folds into a training set and set the rest fold as the test set. We applied our analysis procedure on the training dataset to select predictive voxels and networks. Same tuning parameters  $\tau = 5$ ,  $\alpha = 0.8$  and  $\nu = 20$  were used on each ROI cluster. The selected voxels on 116 ROIs were then pooled together and used to predict the disease status on the test dataset, along with covariates age and sex. We repeated this procedure till each fold has been used as the test set once. The overall classification errors were then computed by summing over all five test sets. The prediction results are summarized in Table 3. For comparison, we also reported prediction results from (i) marginal linear discriminant analysis (LDA), which assumes all voxels are independent (unconnected), (ii) sure independent screening (SIS)<sup>49,50</sup>, and (iii) iterative sure independent screening (ISIS)<sup>50,51</sup>. For SIS and ISIS, logistic regressions were applied on each pair of classes. The class with the highest average predicted probability was assigned to be the final predicted class. Numbers of misclassification are given in Table 3. Our approach gives the smallest prediction errors overall and within each class.

## 5. Discussion

The computational burden of the proposed analysis pipeline is comparable to that from the marginal approaches<sup>49,50</sup>. The major computational cost comes from calculating the whole brain correlation matrix. However, this can be alleviated by parallel computing. The connected component searching could also be computation-intensive if the number of connected voxels to a marginally strong signal is large. In our application, we restricted the length of any connection path in a connected component to be less than 10. This way, only the most closely connected voxels were maintained in a large-sized connected component. The analysis source codes were packed into an R package and can be found at <https://github.com/lygglygg/mLDA>

## Strengths and limitations

The strengths of this study are two-fold. First, it integrates inter-voxel connectivity into neuroimaging signal selection, and makes it possible to select both network-based and marginally weak signals. Secondly, different to many principal component analyses in neuroimaging association studies, our approach can select neuropathologically meaningful biomarkers – the local brain networks, while achieving high prediction accuracy.

Accurate estimation for the covariance structures requires greater sample sizes compared to for the mean structures. Breaking down the overall brain connectomic structures onto separate ROI clusters (see Figure 4) may cause loss of information. It is recognized that the inter-voxel connectivity may not fully reveal the connection pattern between neurons.

## Disclosure of Potential Conflicts of Interest

No potential conflicts of interest were disclosed by the authors.

**Table 1.** Top selected voxel signals\*.

voxel	ROI	MW/MS <sup>†</sup>	marginal MD <sup>‡</sup>	network MD <sup>‡</sup>	unadjusted p-value	adjusted p-value
<b>AD-MCI</b>						
vox_5555	Cerebelum_7b_R	MW	0.27	352.34	0:036	NS**
vox_5445	Cerebelum_7b_R	MW	0.16	139.32	0:012	NS
vox_9000	Cerebelum_Crus2_R	MW	0.07	105.08	<1e-5	<0.05
vox_168602	Paracentral_Lobule_L	MW	2.78	105.01	<1e-5	<0.05
vox_78272	Caudate_R	MW	5.37	104.98	<1e-5	<0.05
vox_5890	Cerebelum_7b_R	MW	0.34	104.41	<1e-5	<0.05
vox_173066	Paracentral_Lobule_L	MW	4.62	101.00	<1e-5	<0.05
vox_90518	Insula_L	MS	7.85	82.57	<1e-5	<0.05
vox_131355	Frontal_Sup_Medial_L	MW	3.99	82.20	0:069	NS
vox_90612	Insula_L	MS	7.31	81.73	<1e-5	<0.05
<b>AD-Healthy</b>						
vox_6027	Cerebelum_10_R	MW	1.60	629.64	<1e-5	<0.05
vox_6024	Cerebelum_10_R	MW	1.73	291.60	<1e-5	<0.05
vox_6079	Cerebelum_10_R	MW	2.28	290.65	<1e-5	<0.05
vox_5989	Cerebelum_10_R	MW	1.33	216.92	<1e-5	<0.05
vox_5890	Cerebelum_7b_R	MW	1.28	135.39	0:056	NS
vox_89146	Lingual_R	MW	-1.54	112.60	<1e-5	<0.05
vox_43386	Temporal_Mid_R	MW	-7.89	105.10	<1e-5	<0.05
vox_6058	Cerebelum_10_R	MW	1.79	98.71	<1e-5	<0.05
vox_127104	Precuneus_L	MW	3.70	97.61	<1e-5	<0.05
vox_43299	Temporal_Mid_R	MW	-8.39	95.56	<1e-5	<0.05
<b>MCI-Healthy</b>						
vox_138843	Precuneus_L	MW	-1.95	162.95	<1e-4	NS
vox_145132	Precuneus_L	MW	-0.55	129.85	<1e-5	<0.05
vox_64457	Frontal_Med_Orb_R	MW	-3.09	118.87	<1e-5	<0.05
vox_141950	Parietal_Inf_L	MW	-1.89	107.41	<1e-5	<0.05
vox_36045	Temporal_Mid_R	MW	-3.19	90.40	<1e-5	<0.05
vox_151373	Precuneus_L	MW	0.75	89.75	<1e-5	<0.05
vox_132482	Precuneus_L	MW	-3.57	83.24	<1e-5	<0.05
vox_68201	Frontal_Med_Orb_R	MW	-3.49	77.16	<1e-5	<0.05
vox_180609	Paracentral_Lobule_L	MW	1.97	76.12	<1e-5	<0.05
vox_87702	Cingulum_Ant_L	MW	-3.60	68.75	<1e-5	<0.05

\* Selected voxels are ranked by its maximum absolute local-network-adjusted mean difference between a pair of classes in a decreasing order.

† MW: Marginally weak signal. MS: Marginally strong signal.

‡ marginal MD: marginal mean difference. network MD: local network adjusted mean difference.

\*\* NS: Non-significant.



**Table 2:** Top selected local brain networks\*.

top voxel(s)	ROI(s) the network sitting in	MW <sup>†</sup> #	MS <sup>‡</sup> #	Hotelling t- squared statistics	unadjusted network p-value	Adjusted** network p-value	literature evidence
<b>AD-MCI</b>							
vox_168602	Paracentral_Lobule_L	5	1	5.7	6.1e-5	0.01	52,53,54,55
vox_78272	Caudate_R	4	3	3.7	1.8e-3	NS	56,57,58
vox_90518	Olfactory_L	5	1	5.9	4.6e-5	0.008	59,60,53,61
vox_152631	Precentral_R	5	1	4.0	0.0019	NS	52,62,63
<b>AD-Healthy</b>							
vox_6027; vox_5989; vox_6024; vox_5987	Cerebellum_10_L; Cerebellum_10_R	5	3	3.5	0.03	NS	64
vox_89146	Lingual_R; Calcarine_R	5	1	7.5	3.8e-6	0.0005	52,65,66,67,68
vox_32891	Amygdala_L	24	1	4.7	1.6e-8	2.1e-6	69
<b>MCI-Healthy</b>							
vox_138843; vox_145132; vox_151373; vox_132482	Precuneus_L	5	1	8.5	2.7e-7	3.5e-5	70,71,72,73
vox_64457; vox_68201	Frontal_Med_Orb_R	6	1	2.7	0.014	NS	52,74
vox_141950	Parietal_Inf_L	4	3	2.3	0.038	NS	75,76
vox_36045	Temporal_Mid_R	6	1	3.5	0.0016	NS	77,78
<p>* Local brain networks with a significant unadjusted network p-value and host selected informative voxels are listed.</p> <p>** Adjusted p-values are adjusted for the number of local networks selected that differentiate the pair of disease classes.</p> <p>† MW #: number of selected marginally weak signals in the network.</p> <p>‡ MS #: number of selected marginally strong signals in the network.</p>							

**Table 3:** Numbers of mis-classified subjects by different methods.

	<b>AD</b>	<b>MCI</b>	<b>Healthy</b>	<b>total</b>
localNet-LDA	2	7	3	12
LDA	5	28	8	41
SIS-logistic	11	46	26	83
ISIS-logistic	7	48	10	65

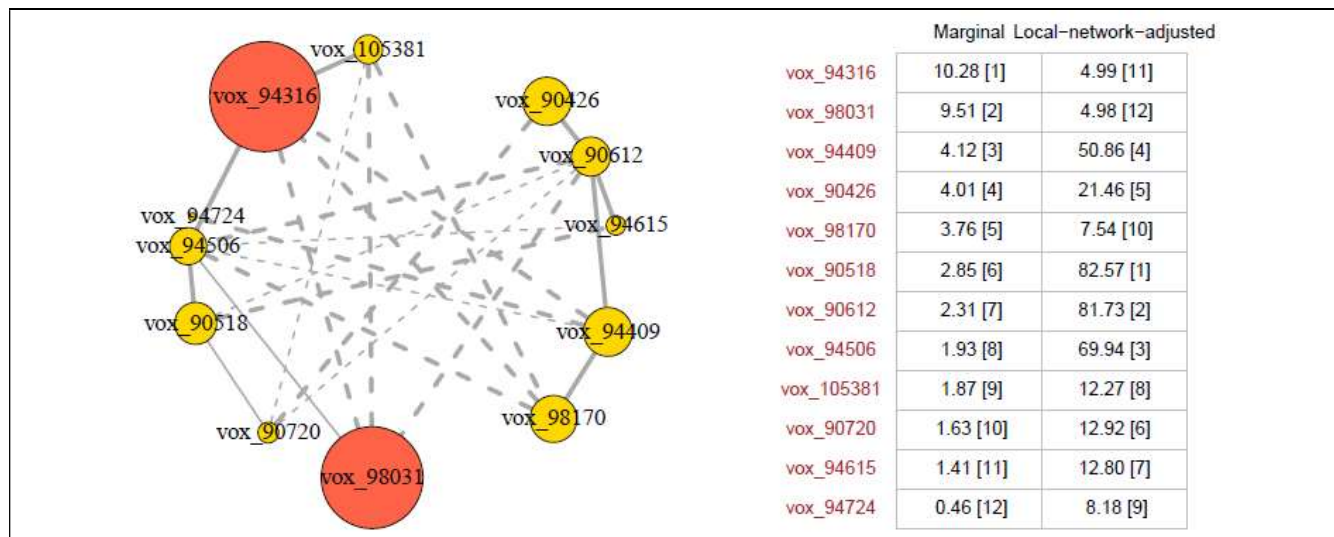


**Figure 1:** Left panel: a local brain-network in cerebellum Crus on the left hemisphere of the brain. Red: marginally detectable (strong) signal. Yellow: marginally undetectable (weak) signals. Solid line: positive connections. Dashed line: negative connections. Line width represents strength of connections. Right panel: Mean differences between the AD and MCI groups. First column: marginal mean differences (divided by the marginal variances). Second column: local network adjusted mean differences. Integers in the brackets are the ranks of the absolute mean differences for the 12 voxels, ranked from the greatest to the smallest.

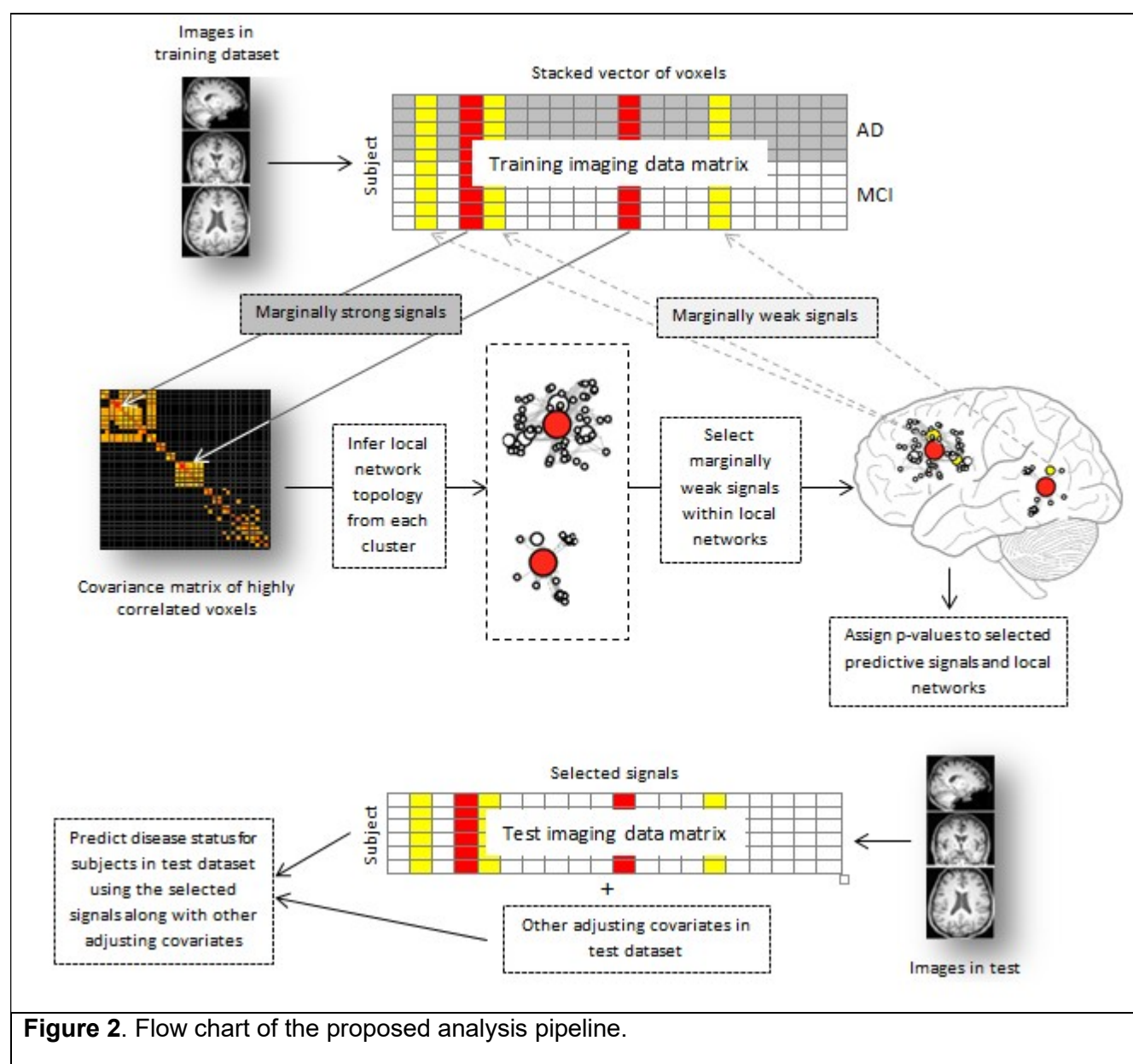


**Figure 2.** Flow chart of the proposed analysis pipeline.

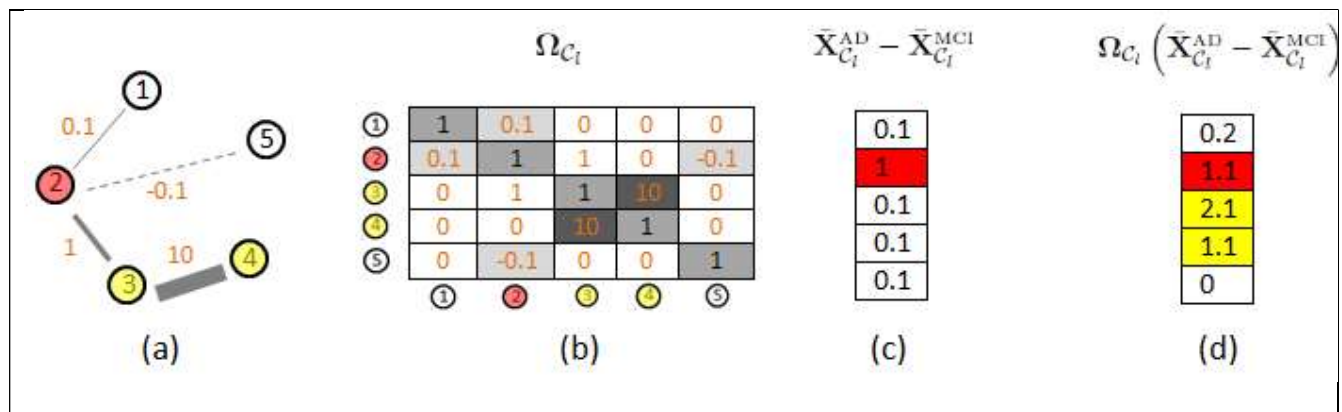
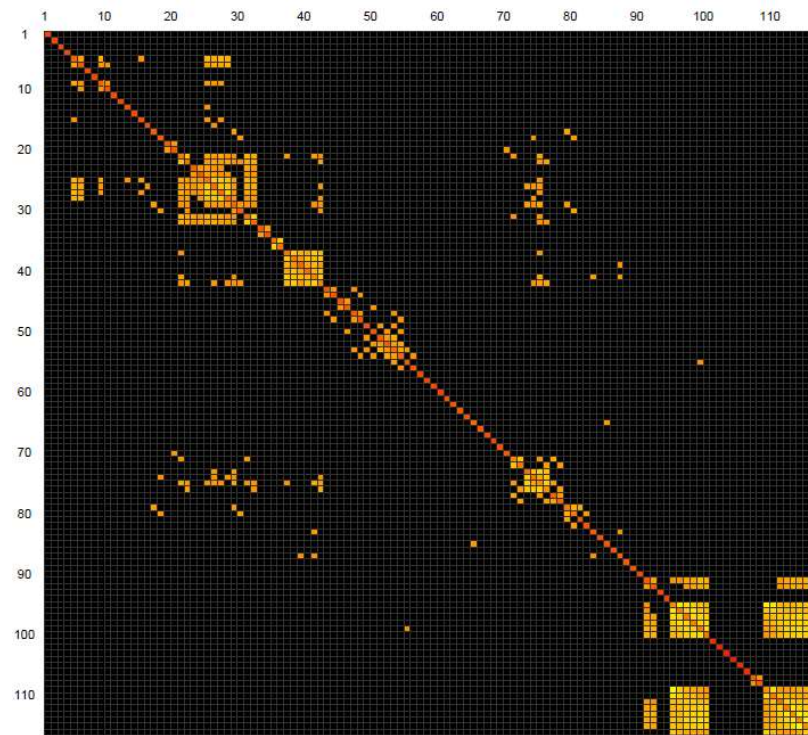
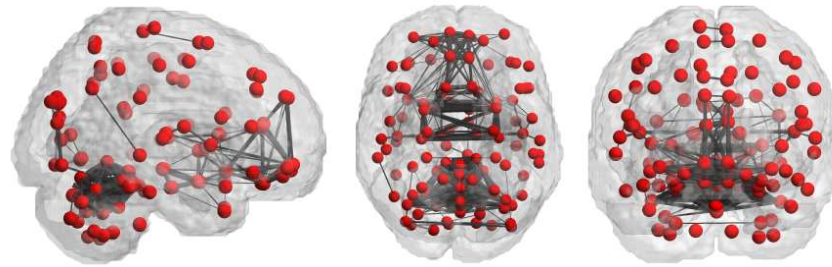


**Figure 3.** A toy example of a local brain network with five voxels. (a) Topology of the network. numbers on each edge are for the edge strength. Negative numbers mean the two voxels are negatively connected. (b) The corresponding precision matrix  $\Omega_{C_l}$ . (c) Marginal differentiating effects between AD and MCI groups. Red: marginally strong signals. (d) Local network adjusted differentiating effects between AD and MCI groups. Yellow: marginally weak signals.



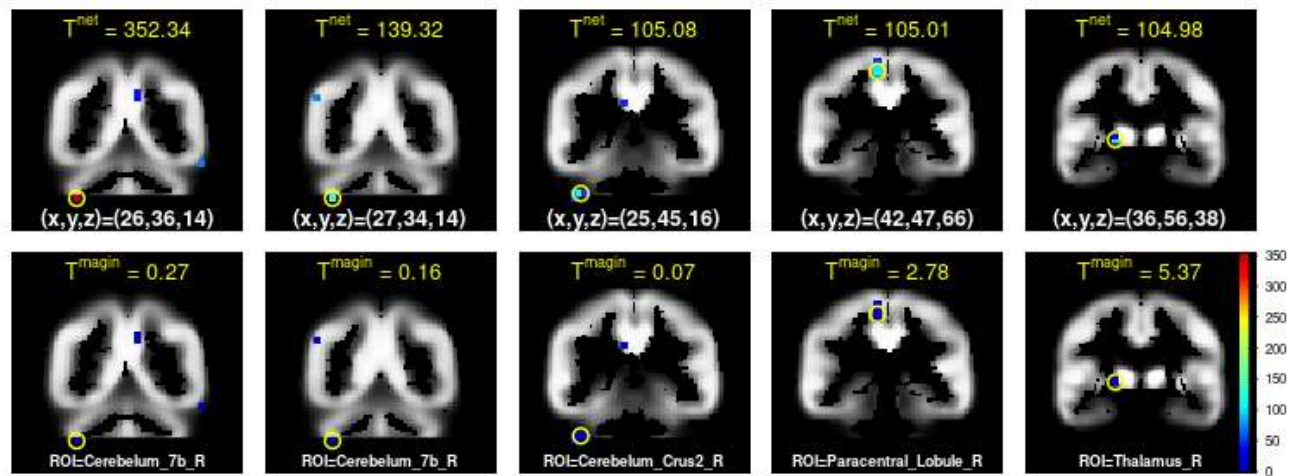
(a)



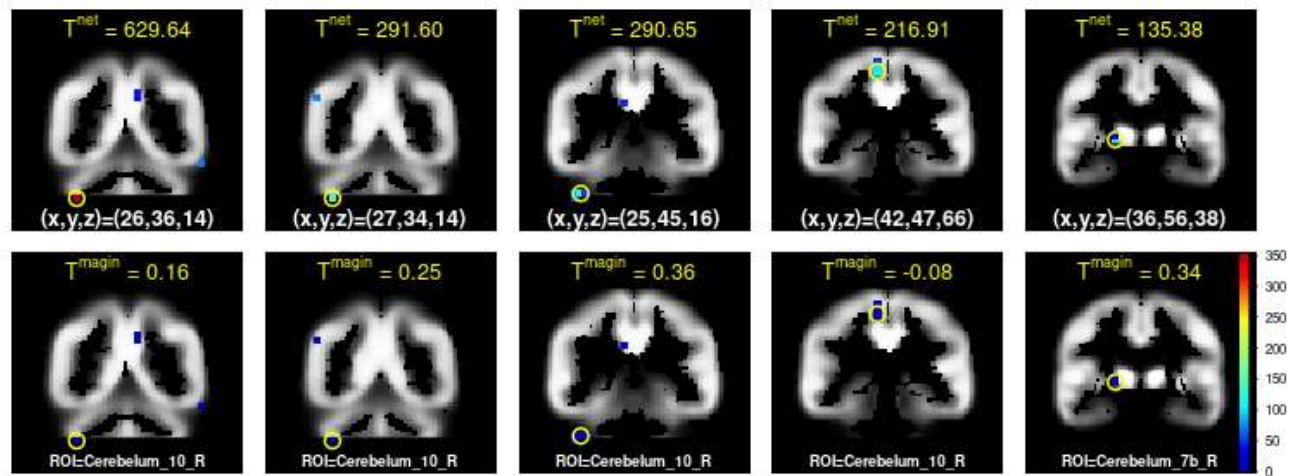
(b)

**Figure 4.** (a) ROI block-wise thresholded sample correlation matrix. A cell represents the weighted  $L_2$  norm of the correlation block between a pair of ROI's (weighted by  $1/\sqrt{v_1 v_2}$  where  $v_1$  and  $v_2$  are the numbers of voxels in the two ROIs, respectively) in the voxel-level correlation matrix. Raw voxel-level correlations are thresholded at 0.8. The weighted  $L_2$  norms are further thresholded at 0.8, which is the median of the 6,670 off-diagonal ROI block  $L_2$  norms. All blocks with  $L_2$  norm  $\leq 0.4$  are set to zero. The black squares represent the zero blocks. The lighted squares are for non-zero blocks. Lighter color indicates greater  $L_2$  norm values. (b) 3D ROI connection topology viewed from sagittal (left), axial (middle) and coronal (right) directions. Each dot represents a central point of an ROI. An edge exists between two ROIs if the corresponding thresholded correlation block is nonzero.

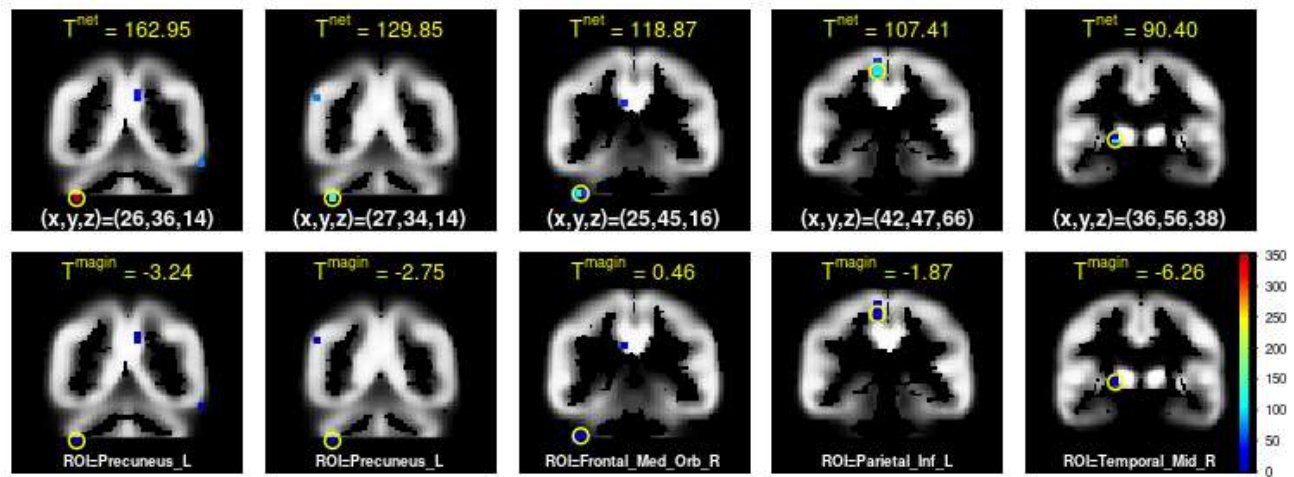




(a) Top five selected voxels differentiating AD and MCI.



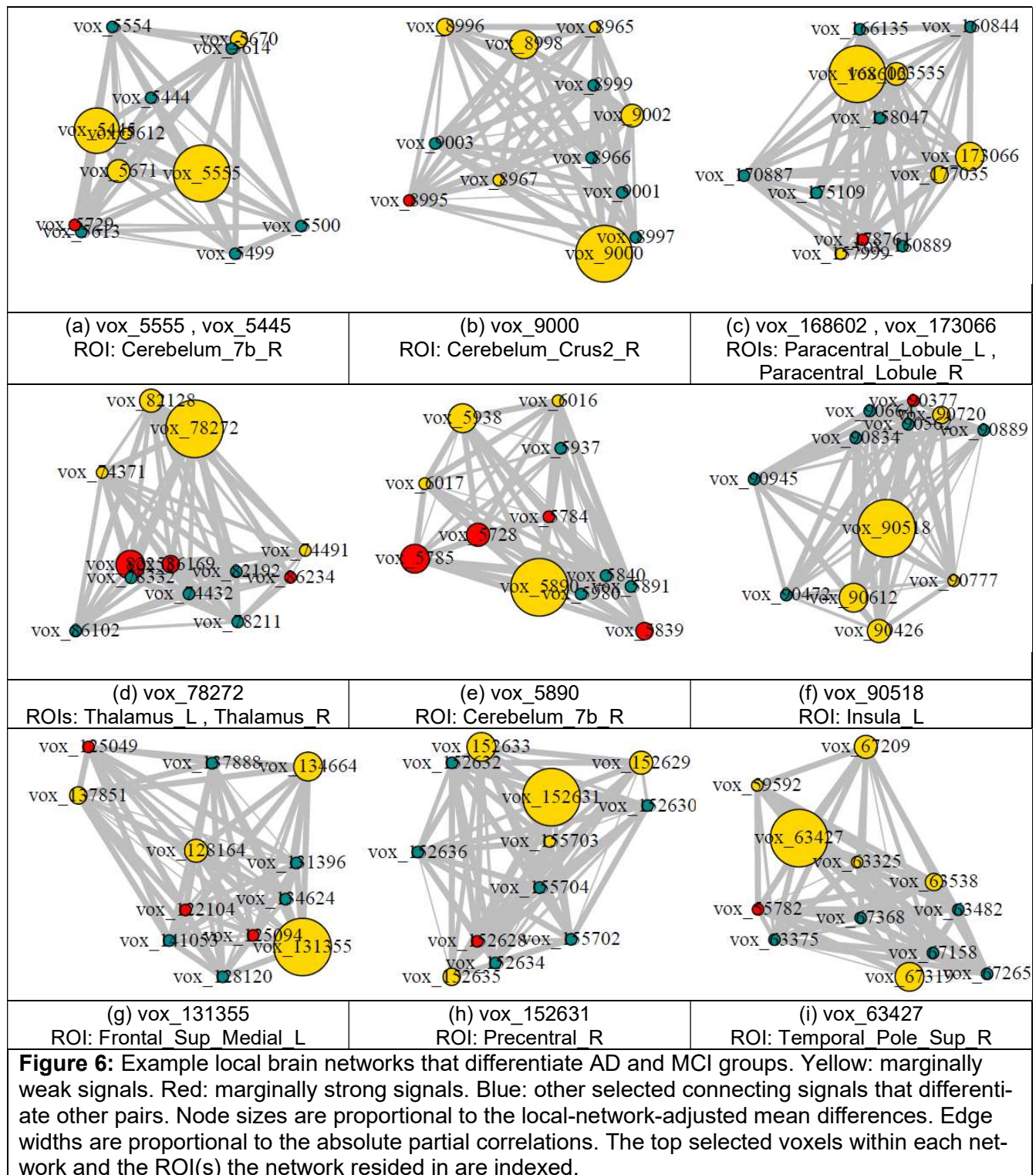
(b) Top five selected voxels differentiating AD and NC.

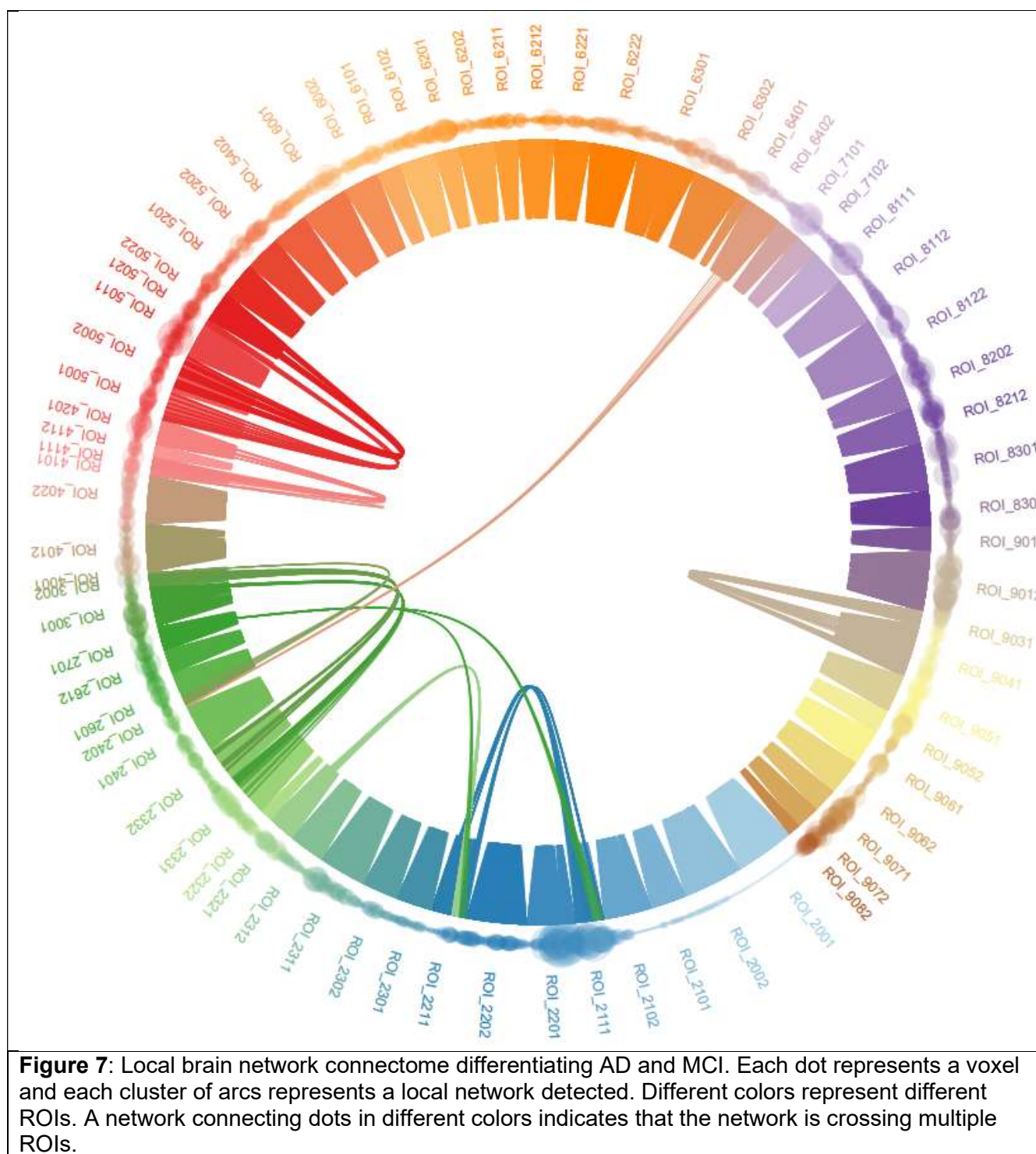


(c) Top five selected voxels differentiating MCI and NC.

**Figure 5:** The symbol  $\hat{T}^{net}$ , defined in equation (3), represents the local network adjusted mean difference between a pair of classes for a voxel. The symbol  $\hat{T}$ , defined in equation (1), represents the marginal mean difference between a pair of classes for a voxel. The triplet (x, y, z) represents the coordinates of the top voxel signal highlighted in yellow circle. ROI gives the regions of interest for the top voxel signal.







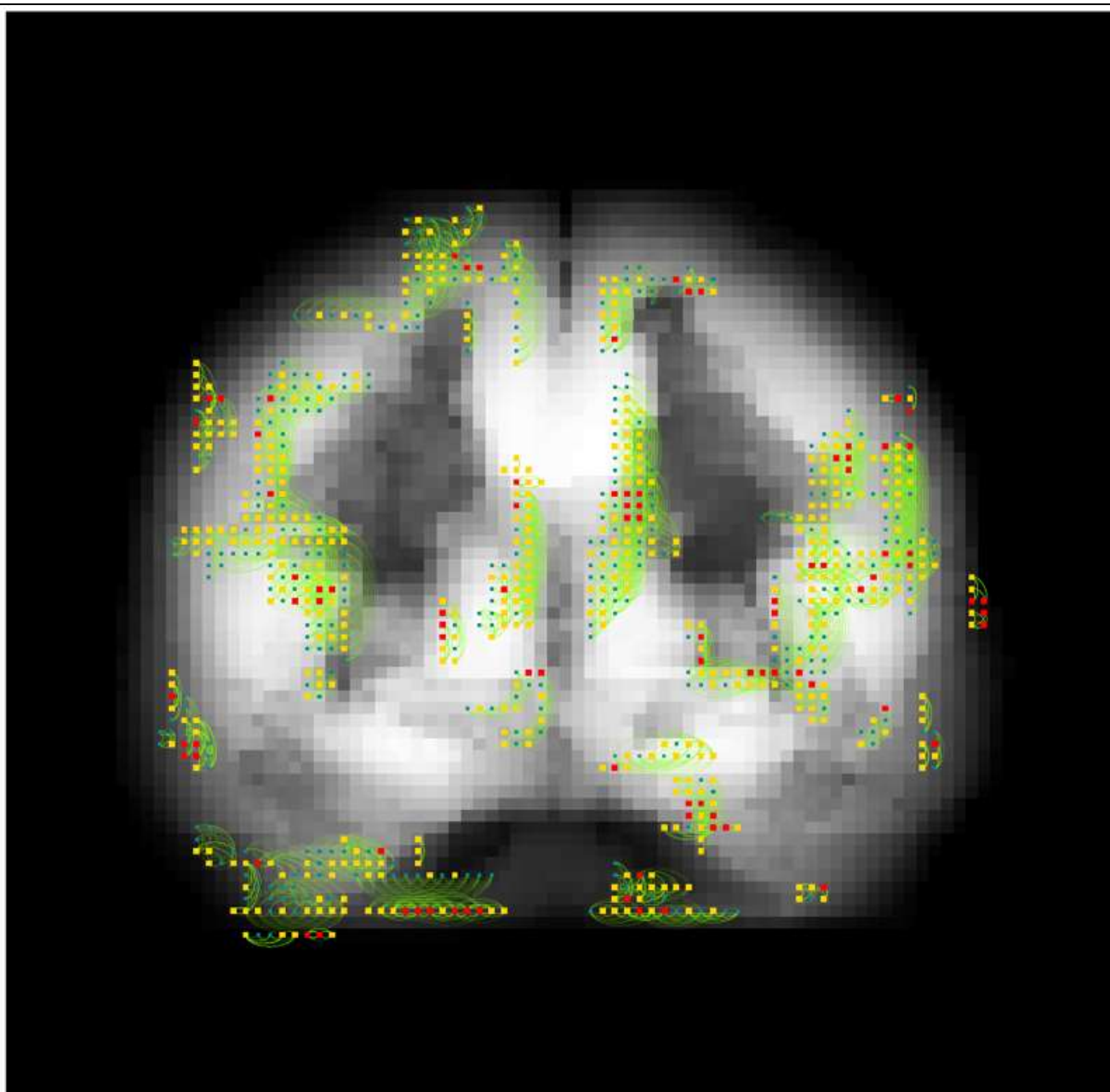


**Figure 8:** Overlaying of the brain network connectome differentiating AD and MCI on the brain. All local networks are projected to a coronal slice of the brain at midline. Red voxel: marginally strong signal. Yellow voxel: marginally weak signal. Blue voxel: non-selected connecting voxel in a selected local brain network (might differentiate other pair of classes).



# References

- <sup>1</sup> James, B. D., Leurgans, S. E., Hebert, L. E., Scherr, P. A., Yaffe, K., and Bennett, D. A. (2014). Contribution of Alzheimer disease to mortality in the United States. *Neurology*, 82(12):1045—1050.
- <sup>2</sup> Xu, J., Murphy, S. L., Kochanek, K. D., Bastian, B., and Arias, E. (2018). Deaths: Final data for 2016. *National Vital Statistics Reports*, 67(5).
- <sup>3</sup> Alzheimer's Association report (2018). 2018 Alzheimer's disease facts and figures. *Alzheimer's Dementia*, 14(3):367—429.
- <sup>4</sup> Alzheimer's association report (2020). 2020 Alzheimer's disease facts and figures. *Alzheimer's Dementia*, 16:391—460.
- <sup>5</sup> Hurd, M. D., Martorell, P., Delavande, A., Mullen, K. J., and Langa, K. M. (2013). Monetary costs of dementia in the united states. *New England Journal of Medicine*, 368(14):1326—1334.
- <sup>6</sup> Gauthier, S., Reisberg, B., Zaudig, M., Peterson, R. C., Ritchie, K., Broich, K., et al. (2006). Mild cognitive impairment. *The Lancet*, 367(9518):1262—1270.
- <sup>7</sup> Markesbery, W. R. (2010). Neuropathologic alterations in mild cognitive impairment: a review. *Journal of Alzheimer's Disease*, 19(1):221—228.
- <sup>8</sup> Mitchell, A. J. and Shiri-Feshki, M. (2009). Rate of progression of mild cognitive impairment to dementia – meta-analysis of 41 robust inception cohort studies. *Acta Psychiatrica Scandinavica*, 119(4):252—265.
- <sup>9</sup> Vos, S. J., Verhey, F., Frolich, L., Kornhuber, J., Wiltfang, J., Maier, W., Peters, O., Ruther, E., Nobili, F., Morbelli, S., et al. (2015). Prevalence and prognosis of Alzheimer's disease at the mild cognitive impairment stage. *Brain*, 138(5):1327—1338.
- <sup>10</sup> A Sanchez-Catasus, C., N Stormezand, G., Jan van Laar, P., P De Deyn, P., Alvarez Sanchez, M., and AJO Dierckx, R. (2017). FDG-PET for prediction of AD dementia in mild cognitive impairment. a review of the state of the art with particular emphasis on the comparison with other neuroimaging modalities (MRI and perfusion SPECT). *Current Alzheimer Research*, 14(2):127—142.
- <sup>11</sup> Brodmann, K. (2010). *Brodmann's Localisation in the Cerebral Cortex*. Springer.
- <sup>12</sup> McKhann, G. M., Knopman, D. S., Chertkow, H., Hyman, B. T., Jack Jr, C. R., Kawas, C. H., Klunk, W. E., Koroshetz, W. J., Manly, J. J., Mayeux, R., et al. (2011). The diagnosis of dementia due to Alzheimer's disease: Recommendations from the national institute on aging-Alzheimer's association workgroups on diagnostic guidelines for Alzheimer's disease. *Alzheimer's , Dementia*, 7(3):263—269.
- <sup>13</sup> Mueller, S. G., Weiner, M. W., Thal, L. J., Petersen, R. C., Jack, C. R., Jagust, W., Trojanowski, J. Q., Toga, A.W., and Beckett, L. (2005). Ways toward an early diagnosis in Alzheimer's disease: the Alzheimer's Disease Neuroimaging Initiative (ADNI). *Alzheimer's , Dementia*, 1(1):55—66.
- <sup>14</sup> Albert, M. S., DeKosky, S. T., Dickson, D., Dubois, B., Feldman, H. H., Fox, N. C., Gamst, A., Holtman, D. M., Jagust, W. J., Petersen, R. C., Snyder, P. J., Carrillo, M. C., Thies, B., and Phelps, C. H. (2011). The diagnosis of mild cognitive impairment due to Alzheimer's disease: recommendations from the national institute on aging-Alzheimer's association workgroups on diagnostic guidelines for Alzheimer's disease. *The Journal of the Alzheimer's Association*, 7(3):270—279.
- <sup>15</sup> Garibotto, V., Herholz, K., Boccardi, M., Picco, A., Varrone, A., Nordberg, A., Nobili, F., Ratib, O., for the Roadmap, G. T. F., et al. (2017). Clinical validity of brain uorodeoxyglucose positron emission tomography as a biomarker for Alzheimer's disease in the context of a structured 5-phase development framework. *Neurobiology of Aging*, 52:183—195.
- <sup>16</sup> Hoffman, J. M., Welsh-Bohmer, K. A., Hanson, M., Crain, B., Hulette, C., Earl, N., and Coleman, R. E. (2000). FDG PET imaging in patients with pathologically verified dementia. *J Nucl Med*, 41:1920—1928.

- <sup>17</sup> Wee, C.-Y., Yap, P.-T., Shen, D., and Alzheimer's Disease Neuroimaging Initiative (2013). Prediction of Alzheimer's disease and mild cognitive impairment using cortical morphological patterns. *Human Brain Mapping*, 34(12):3411—3425.
- <sup>18</sup> Jack Jr, C. R., Bennett, D. A., Blennow, K., Carrillo, M. C., Dunn, B., Haeberlein, S. B., et al. (2018). NIA-AA research framework: Toward a biological definition of Alzheimer's disease. *Alzheimer's Dementia*, 14(4):535—562.
- <sup>19</sup> Frisoni, G. B., Fox, N. C., Jack, C. R., Scheltens, P., and Thompson, P. M. (2010). The clinical use of structural MRI in Alzheimer disease. *Nature Reviews Neurology*, 6:67—77.
- <sup>20</sup> Lowe, V. J., Bruinsma, T. J., Wiste, H. J., Min, H.-K., Weigand, S. D., Fang, P., Senjem, M. L., Theneau, T. M., Boeve, B. F., Josephs, K. A., Pandey, M. K., Murray, M. E., Kantarci, K., Jones, D. T., Vemuri, P., Graack, J., Schwarz, C. G., Machulda, M. M., Mielke, M. M., Roberts, R. O., Knopman, D. S., Petersen, R. C., and Jack, C. R. (2019). Cross-sectional associations of tau-pet signal with cognition in cognitively unimpaired adults. *Neurology*, 93(1):29—39.
- <sup>21</sup> Scheltens, P., Fox, N. C., Barkhof, F., and De Carli, C. (2002). Structural magnetic resonance imaging in the practical assessment of dementia: beyond exclusion. *The Lancet Neurology*, 1:13—21.
- <sup>22</sup> Coppersmith, D. and Winograd, S. (1990). Matrix multiplication via arithmetic progressions. *Journal of Symbolic Computation*, 9(3):251.
- <sup>23</sup> Delbeuck, X., Van der Linden, M., and Collette, F. (2003). Alzheimer's disease as a disconnection syndrome? *Neuropsychology Review*, 13(2):79—92.
- <sup>24</sup> Zhou, J., Gennatas, E. D., Kramer, J. H., Miller, B. L., and Seeley, W. W. (2012). Predicting regional neurodegeneration from the healthy brain functional connectome. *Neuron*, 73(6):1216—1227.
- <sup>25</sup> Contreras, J. A., Goni, J., Risacher, S. L., Sporns, O., and Saykin, A. J. (2015). The structural and functional connectome and prediction of risk for cognitive impairment in older adults. *Current Behavioral Neuroscience Reports*, 2(4):234—245.
- <sup>26</sup> Craddock, R. C., James, G. A., Holtzheimer III, P. E., Hu, X. P., and Mayberg, H. S. (2012). A whole brain fMRI atlas generated via spatially constrained spectral clustering. *Human Brain Mapping*, 33(8):1914—1928.
- <sup>27</sup> Li, Y., Yao, Z., Zhang, H., and Hu, B. (2018). Indirect relation based individual metabolic network for identification of mild cognitive impairment. *J Neurosci Methods*, 309:188—198.
- <sup>28</sup> Parker, D. B. and Razlighi, Q. R. (2019). Task-evoked negative bold response and functional connectivity in the default mode network are representative of two overlapping but separate neurophysiological processes. *Sci Rep*, 9(1):14473.
- <sup>29</sup> Shen, X., Tokoglu, F., Papademetris, X., and Constable, R. T. (2013). Groupwise whole-brain parcellation from resting-state fMRI data for network node identification. *NeuroImage*, 82:403—415.
- <sup>30</sup> Guest, O. and Love, B. C. (2017). What the success of brain imaging implies about the neural code. *eLife*, 6:e21397.
- <sup>31</sup> Kriegeskorte, N., Cusack, R., and Bandettini, P. (2010). How does an fMRI voxel sample the neuronal activity pattern: compact-kernel or complex spatiotemporal filter? *NeuroImage*, 49(3):1965—1976.
- <sup>32</sup> Lee, G., Nho, K., Kang, B., et al. (2019). Predicting Alzheimer's disease progression using multi-modal deep learning approach. *Sci Rep*, 9:1952.
- <sup>33</sup> Li, J., Zhang, Q., Chen, F., Yan, J., Kim, S., Wang, L., Feng, W., Saykin, A. J., Liang, H., and Shen, L. (2015). Interactions explain variance in cingulate Amyloid burden: An AV-45 PET genome-wide association and interaction study in the ADNI cohort. *BioMed research international*, 647389.
- <sup>34</sup> Ridge, P., Mukherjee, S., Crane, P., Kauwe, J., and Consortium, A. D. G. (2013). Alzheimer's disease: analyzing the missing heritability. *PLoS ONE*, 8(11):e79771.
- <sup>35</sup> Li, Y., Hong, H. G., Ahmed, E., and Li, Y. (2019a). Weak signals in high-dimensional regression: Detection, estimation and prediction. *Appl. Stochastic Models Bus., Ind.*, 35(2):283—298.

- <sup>36</sup> Li, Y., Hong, H. G., and Li, Y. (2019b). Multiclass linear discriminant analysis with ultrahigh-dimensional features. *Biometrics*, 75(4):1086—1097.
- <sup>37</sup> Bickel, P. and Levina, E. (2008). Covariance regularization by thresholding. *Ann. Statist.*, 36(6):2577—2604.
- <sup>38</sup> Fan, J., Liao, Y., and Min, M. (2011). High-dimensional covariance matrix estimation in approximate factor models. *Ann. Statist.*, 39(6):3320—3356.
- <sup>39</sup> Shapiro, L. and Stockman, G. (2002). *Computer Vision*. Prentice Hall.
- <sup>40</sup> Subramanian, A., Tamayo, P., Mootha, V. K., Mukherjee, S., Ebert, B. L., Gillette, M. A., Paulovich, A., Pomeroy, S. L., Golub, T. R., Lander, E. S., and Mesirov, J. P. (2005). Gene set enrichment analysis: A knowledge-based approach for interpreting genome-wide expression profiles. *Proceedings of the National Academy of Sciences*, 102(43):15545—15550.
- <sup>41</sup> Wu, M. C., Zhang, L., Wang, Z., Christiani, D. C., and Lin, X. (2009). Sparse linear discriminant analysis for simultaneous testing for the significance of a gene set/pathway and gene selection. *Bioinformatics*, 25(9):1145—1151.
- <sup>42</sup> Jack, C. R. J., Bernstein, M. A., Fox, N. C., Thompson, P., Alexander, G., Harvey, D., et.al. (2008). The Alzheimer's disease neuroimaging initiative (ADNI): MRI methods. *Journal of magnetic resonance imaging*. *JMRI*, 27(4):685—691.
- <sup>43</sup> Moon, S.W., Dinov, I. D., Hobel, S., Zamanyan, A., Choi, Y. C., Shi, R., Thompson, P. M., Toga, A. W., and Initiative, A. D. N. (2015). Structural brain changes in early-onset Alzheimer's disease subjects using the LONI pipeline environment. *Journal of neuroimaging: official journal of the American Society of Neuroimaging*, 25(5):728—737.
- <sup>44</sup> Weiner, M. W. and Veitch, D. P. (2015). Introduction to special issue: Overview of Alzheimer's disease neuroimaging initiative. *Alzheimer's , Dementia*, 11(7):730—733.
- <sup>45</sup> Tzourio-Mazoyer, N., Landeau, B., Papathanassiou, D., Crivello, F., Etard, O., Delcroix, N., Mazoyer, B., and Joliot, M. (2002). Automated anatomical labeling of activations in SPM using a macroscopic anatomical parcellation of the mni MRI single-subject brain. *NeuroImage*, 15(1):273—289.
- <sup>46</sup> Li T, Liao Z, Mao Y, Hu J, Le D, Pei Y, Sun W, Lin J, Qiu Y, Zhu J, Chen Y, Qi C, Ye X, Su H, Yu E. Temporal dynamic changes of intrinsic brain activity in Alzheimer's disease and mild cognitive impairment patients: a resting-state functional magnetic resonance imaging study. *Ann Transl Med* 2021;9(1):63. doi: 10.21037/atm-20-7214.
- <sup>47</sup> Bathini, P., Mottas, A., Jaquet, M., Brai, E., Alberi, L. (2019). Progressive signaling changes in the olfactory nerve of patients with Alzheimer's disease. *Neurobiology of Aging*, 76:80—95.
- <sup>48</sup> Yang, H., Xu, H., Li, Q., Jin, Y., Jiang, W., Wang, J., Wu, Y., Li, W., Yang, C., Li, X., Xiao, S., Shi, F., & Wang, T. (2019). Study of brain morphology change in Alzheimer's disease and amnesic mild cognitive impairment compared with normal controls. *General psychiatry*, 32(2), e100005. <https://doi.org/10.1136/gpsych-2018-100005>.
- <sup>49</sup> Fan, J. and Lv, J. (2008). Sure independence screening for ultrahigh dimensional feature space (with discussion). *Journal of Royal Statistical Society B*, 70:849—911.
- <sup>50</sup> Fan, J. and Song, R. (2010). Sure independence screening in generalized linear models with np-dimensionality. *The Annals of Statistics*, 38(6):3567—3604.
- <sup>51</sup> Zhong, W. and Zhu, L. (2015). An iterative approach to distance correlation-based sure independence screening. *Journal of Statistical Computation and Simulation*, 85(11):2331—2345.
- <sup>52</sup> Yao, Z., Zhang, Y., Lin, L., Zhou, Y., Xu, C., Jiang, T., and et al. (2010). Abnormal cortical networks in mild cognitive impairment and Alzheimer's disease. *PLoS Comput Biol*, 6(11):e1001006.
- <sup>53</sup> Li, Y., Wang, Y., Wu, G., Shi, F., Zhou, L., Lin, W., Shen, D., and Alzheimer's Disease Neuroimaging Initiative (2012). Discriminant analysis of longitudinal cortical thickness changes in Alzheimer's disease using dynamic and network features. *Neurobiol Aging*, 33(2):427.e15—30.

- <sup>54</sup> Chen, X., Zhang, H., Zhang, L., Shen, C., Lee, S. W., and Shen, D. (2017). Extraction of dynamic functional connectivity from brain grey matter and white matter for MCI classification. *Hum Brain Mapp.*, 38(10):5019—5034.
- <sup>55</sup> Li, Y., Liu, J., Gao, X., Jie, B., Kim, M., Yap, P.-T., Wee, C.-Y., and Shen, D. (2019). Multimodal hyper-connectivity of functional networks using functionally-weighted lasso for MCI classification. *Medical Image Analysis*, 52:80—96.
- <sup>56</sup> Madsen, S., Ho, A., Hua, X., Saharan, P., Toga, A., Jack, C., Weiner, M., and Thompson, P. (2010). 3d maps localize caudate nucleus atrophy in 400 alzheimer's disease, mild cognitive impairment, and healthy elderly subjects. *Neurobiology of Aging*, 31(8):1312—1325.
- <sup>57</sup> Liu, Y., Pajanen, T., Zhang, Y., Westman, E., Wahlund, L.-O., Simmons, A., Tunnard, C., Sobow, T., Mecocci, P., Tsolaki, M., Vellas, B., Muehlboeck, S., Evans, A., Spenger, C., Lovestone, S., and Soininen, H. (2011). Combination analysis of neuropsychological tests and structural MEI measures in differentiating AD, MCI and control groups – the addneuromed study. *Neurobiology of Aging*, 32(7):1198—1206.
- <sup>58</sup> Elshafey, R., Hassanien, O., Khalil, M., Allah, M. R., Saad, S., Baghdadi, M., and El Zayady, M. (2014). Hippocampus, caudate nucleus and entorhinal cortex volumetric MRI measurements in discrimination between Alzheimer's disease, mild cognitive impairment, and normal aging. *The Egyptian Journal of Radiology and Nuclear Medicine*, 45(2):511—518.
- <sup>59</sup> Vasavada, M. M., Wang, J., Eslinger, P. J., Gill, D. J., Sun, X., Karunanayaka, P., and Yang, Q. X. (2015). Olfactory cortex degeneration in Alzheimer's disease and mild cognitive impairment. *J. Alzheimer's Dis.*, 45(3):947—958.
- <sup>60</sup> Zou, Y. M., Lu, D., Liu, L. P., Zhang, H. H., and Zhou, Y. Y. (2016). Olfactory dysfunction in Alzheimer's disease. *Neuropsychiatric disease and treatment*, 12:869—875.
- <sup>61</sup> Murphy, C. (2019). Olfactory and other sensory impairments in Alzheimer disease. *Nature Reviews Neurology*, 15:11—24.
- <sup>62</sup> Wang, M., Yan, Z., and Jiang, J. (2019). Brain metabolic connectome classify mild cognitive impairment into alzheimer's dementia. *Annu Int Conf IEEE Eng Med Biol Soc.*, 32—35.
- <sup>63</sup> Singh, V., Chertkow, H., Lerch, J. P., Evans, A. C., Dorr, A. E., and Kabani, N. J. (2006). Spatial patterns of cortical thinning in mild cognitive impairment and Alzheimer's disease. *Brain*, 129(11):2885—2893.
- <sup>64</sup> Thomann, P. A., Schlafer, C., Seidl, U., Santos, V. D., Essig, M., and Schroder, J. (2008). The cerebellum in mild cognitive impairment and Alzheimer's disease – a structural MRI study. *Journal of Pschiatric Research*, 42(14):1198—1202.
- <sup>65</sup> Liang, P., Xiang, J., Liang, H., Qi, Z., Li, K., and Alzheimer's Disease NeuroImaging Initiative (2014). Altered amplitude of low-frequency uctuations in early and late mild cognitive impairment and Alzheimer's disease. *Curr Alzheimer Res.*, 11(4):389—398.
- <sup>66</sup> Willette, A. A., Calhoun, V. D., Egan, J. M., and Kapogiannis, D. (2014). Prognostic classification of mild cognitive impairment and Alzheimer's disease: MRI independent component analysis. *Psychiatry Research: Neuroimaging*, 224(2):81—88.
- <sup>67</sup> Liu, X., Bai, F., Yue, C., Shi, Y., Yu, H., Luo, B., and Zhang, Z. (2014). The association between TOMM40 gene polymorphism and spontaneous brain activity in amnesic mild cognitive impairment. *Journal of Neurology*, 261:1499--1507.
- <sup>68</sup> Long, X., Zhang, L., Liao, W., Jiang, C., Qiu, B., and Alzheimer's Disease Neuroimaging Initiative (2013). Distinct laterality alterations distinguish mild cognitive impairment and Alzheimer's disease from healthy aging: statistical parametric mapping with high resolution MRI. *Hum Brain Map*, 34(12):3400—3410.
- <sup>69</sup> Iaccarino, L., Sala, A., Caminiti, S-P, Presotto, L., Perani, D., and Alzheimer's Disease Neuroimaging Initiative (2020) In Vivo MRI Structural and PET Metabolic Connectivity Study of Dopamine Pathways in Alzheimer's Disease. *Journal of Alzheimer's Disease*, 7(3):1003—1016.
- <sup>70</sup> Bailly, M., Destrieux, C., Hommet, C., Mondon, K., Cottier, J.-P., Beauls, E., Vierron, E., Vercouillie, J., Ibazizene, M., Voisin, T., Payoux, P., Barrse, L., Camus, V., Guilloteau, D., and Ribeiro, M.-J. (2015). Precuneus and cingulate cortex

atrophy and hypometabolism in patients with Alzheimer's disease and mild cognitive impairment: MRI and 18f-FDG PET quantitative analysis using freesurfer. *BioMed Research International*. doi: 10.1155/2015/583931.

<sup>71</sup> Rombouts, S. A., Barkhof, F., Goekoop, R., Stam, C. J., and Scheltens, P. (2005). Altered resting state networks in mild cognitive impairment and mild Alzheimer's disease: an fMRI study. *Hum Brain Mapp*, 26(4):231—239.

<sup>72</sup> Ikonomic, M. D., Klunk, W. E., Abrahamson, E. E., J. Wu, C. A. M., Scheff, S. W., Mufson, E. J., and DeKosky, S. T. (2011). Precuneus amyloid burden is associated with reduced cholinergic activity in Alzheimer disease. *Neurology*, 77(1):39—47.

<sup>73</sup> Mattioli, P., Pardini, M., Fama, F., et al. (2021). Cuneus/precuneus as a central hub for brain functional connectivity of mild cognitive impairment in idiopathic rem sleep behavior patients. *Eur J Nucl Med Mol Imaging*. 48(9):2834—2845. doi: 10.1007/s00259-021-05205-6.

<sup>74</sup> Gupta, Y., Kim, J.-I., Kim, B. C., and Kwon, G.-R. (2020). Classification and graphical analysis of Alzheimer's disease and its prodromal stage using multimodal features from structural, diffusion, and functional neuroimaging data and the *APOE* genotype. *Frontiers in Aging Neuroscience*, 12:238.

<sup>75</sup> Greene, S. J. and Killiany, R. J. (2010). Subregions of the inferior parietal lobule are affected in the progression to Alzheimer's disease. *Neurobiology of Aging*, 31(8):1304—1311.

<sup>76</sup> Owen, J. B., Di Domenico, F., Sultana, R., Perluigi, M., Cini, C., Pierce, W. M., and Butterfield, D. A. (2009). Proteomics-determined differences in the concanavalin-a-fractionated proteome of hippocampus and inferior parietal lobule in subjects with Alzheimer's disease and mild cognitive impairment: implications for progression of ad. *J Proteome Res.*, 8(2):471—482.

<sup>77</sup> Convit, A., de Asis, J., de Leon, M. J., Tarshish, C. Y., De Santi, S., and Rusinek, H. (2000). Atrophy of the medial occipitotemporal, inferior, and middle temporal gyri in non-demented elderly predict decline to Alzheimer's disease. *Neurobiol Aging*, 21(1):19—26.

<sup>78</sup> De Santi, S., de Leon, M. J., Rusinek, H., Convit, A., Tarshish, C. Y., Roche, A., Tsui, W. H., Kandil, E., Boppana, M., Daisley, K., Wang, G. J., Schlyer, D., and Fowler, J. (2001). Hippocampal formation glucose metabolism and volume losses in MCI and AD. *Neurobiology of Aging*, 22(4):529—539.